The Exploration of a Novel Terrestrial Analogue for Spaceflight Associated Neuro-ocular Syndrome

Thesis

Presented in Partial Fulfillment of the Requirements for the Degree Master of Science in the Graduate School of The Ohio State University

By

Hayley Samson, B.S

Graduate Program in Vision Science

The Ohio State University

2024

Thesis Committee

Phillip Yuhas, OD, PhD, Co-Advisor

Cynthia Roberts, PhD, Co-Advisor

Nicklaus Fogt, OD, PhD

Jennifer Fogt, OD, MS

Abstract

Purpose: Spaceflight Associated Neuro-ocular Syndrome (SANS) is experienced by astronauts in microgravity and is characterized by a hyperopic shift, globe flattening, optic disc edema and choroidal folds. The pathophysiology of SANS is not yet known, but it is thought to be caused by the loss of ground-based hydrostatic pressure gradient, which results in a head-ward fluid shift. It has been recently hypothesized that this fluid shift elicits congestion of the orbital fat. Thyroid eye disease (TED) may be a novel terrestrial analog to SANS because the physical manifestations in both pathologies can be similar. The purpose of this study is to assess the performance of an established magnetic resonance imaging (MRI) sequence to measure fat/water fractions in the orbit, first in phantoms and then in one initial TED subject.

Methods: Fat-water fractions in orbital phantoms were quantified using a q-Dixon Multi-Echo Chemical Shift Encoded MRI at 3 Tesla. Images were acquired in triplicate to evaluate test-retest reliability, as well as in 3 orientations. The first subject with TED was enrolled, provided informed consent, and triplicate orbital images were acquired. These images were processed with the imaging software ImageJ and orbital fat volume and fat fraction measurements were obtained from selected orbital fat.

Results: The MRI sequence measured fat-fraction in the phantom models with good accuracy, and there was a strong linear association in all three positions between

measured fat values and true fat values ($R^2 = 0.9978$). The sequence was found to be repeatable, with good test-retest reliability between the positions and with triplicate acquisitions. Preliminary results for the initial TED subject show successful procurement of overall average fat-fraction (approximately 43% fat in the right orbit and 42% in the left orbit). Statistical analysis suggests generally good agreement between the triplicate scans, with low coefficient of variation in both orbits (6% in the right orbit, 7% in the left orbit). The difference in fat fraction between the two orbits of the subject was not significant.

Conclusions: q-Dixon MRI sequencing was validated in ideal conditions through phantom models. Results showed good accuracy and repeatability with the phantoms. Successful imaging and quantification of fat-water fractions in the initial TED subject shows promising results for study of orbital congestion in TED. These results are favorable towards the future exploration of TED as a ground-based analog for SANS.

Dedication

To my family and friends that have supported and encouraged me throughout it all.

Acknowledgments

Many thanks to:

My advisors Dr Phillip Yuhas and Dr Cynthia Roberts for their great help, insight, and encouragement.

Dr Nicklaus Fogt and Dr Jennifer Fogt for sitting on my defense committee.

Dr Katelyn Swindle-Reilly for her help in creating and preparing orbital phantoms.

Dr Orlando Simonetti and Yue Pan for their help in imaging of orbital phantoms and our initial subject.

Hayley Griggs, Krupa Patel and all of the crew at Havener Eye Institute that aided participant study visits.

Vita

2016	……	The Seven Hills School Cincinnati, OH
2019	……	NIFS NASA Langley Research Center, Summer Intern Hampton, VA
2020	……	Bachelor of Science (Medical Science) *Magna Cum Laude, Honors Scholar* University of Cincinnati, College of Medicine Cincinnati, OH
2024	……..	Doctor of Optometry The Ohio State University, College of Optometry Columbus, OH
2024	……...	Master of Vision Science The Ohio State University, College of Optometry Columbus, OH

Fields of Study

Major Field: Vision Science

Table of Contents

Abstract ii
Dedication iv
Acknowledgments v
Vita vi
List of Tables ix
List of Figures x
Chapter 1. Introduction 1
Spaceflight Associated Neuro-ocular Syndrome 2
Terrestrial Analogue of SANS 14
Measurement of Orbital Fat 17
Purpose 21
Chapter 2. Methods 23
Phantom Construction 23
Sequence Validation 27
Human Experiments 29
Participants 29
MRI Imaging and Data Collection 29
MR Image Processing 30
Statistical Analysis 33
Phantom Experiments 33
Human Experiments 33
Chapter 3. Results 35
Phantom Model Results 35
Preliminary Human Subject Results 39
Chapter 4. Discussion 47
Study Goals 47
Phantom Model Validation 47
Preliminary Human Subject Imaging 49

Measurements of Orbital Congestion in TED and the Potential for Use in SANS 54
Limitations 55
Conclusion and Future Study 56

List of Tables

Table 1. Comparison of TED and SANS Known Presentations..... 16
Table 2. Fat-water Fractions of the Model Phantoms..... 24
Table 3. Accuracy of Phantoms in Three Orientations..... 36
Table 4. Right Orbit Fat Fraction and Orbital Fat Volume Measured..... 40
Table 5. Left Orbit Fat Fraction and Orbital Fat Volume Measured..... 41

List of Figures

Figure 1. SANS Hypothesized Pathophysiologies Flow Chart 5
Figure 2. Orbital Congestion..... 11
Figure 3. Examples of Fat-Water Phantoms..... 26
Figure 4. Orientation of Phantom Models in the Scanner 28
Figure 5. Example of Retrobulbar Fat Region of Interest Measured..... 31
Figure 6. Example Region of Interest Selection Process..... 32
Figure 7. Absolute Average Deviation from True Fat Fraction Values 37
Figure 8. Measured versus True Fat Value..... 38
Figure 9. Right Orbit Fat Fraction by Scan..... 40
Figure 10. Left Orbit Fat Fraction by Scan..... 41
Figure 11. Right Orbit vs Left Orbit Fat Volume..... 42
Figure 12. Right Orbit vs Left Orbit Fat Fraction..... 43
Figure 13. Right Orbit Fat Fraction Profile 45
Figure 14. Left Orbit Fat Fraction Profile..... 46
Figure 15. Demonstration of Misaligned Head..... 51

Chapter 1. Introduction

One of the hallmarks of the twentieth century was the attainment of space flight, and the desire for human exploration of space continues to the present. Although it has been years since the National Aeronautics and Space Administration (NASA) has conducted manned spaceflight missions using its own spacecraft, NASA astronauts still routinely complete extended missions aboard the International Space Station (ISS), shuttling to and from the ISS using the spacecraft of other nations or of private companies. In the upcoming decades, the agency aims to return to the moon and to launch a manned expedition to Mars that will last at least three years. Beyond government-sponsored missions, there has been a dramatic increase in the commercialization of spaceflight. Companies such as SpaceX, Virgin Galactic, and Blue Origin have succeeded in sending humans into space, and the demand for recreational spaceflights is growing. Given the increased frequency and the longer duration of manned spaceflights, both in the private and in the public sectors, there is an urgent need to study the risks to the human body that accompany prolonged exposure to microgravity environments.

There are many risks associated with spaceflight, especially long-duration missions. For example, radiation exposure and alterations to diet have the potential to undermine human health. Long-term exposure to microgravity, or the condition in which

gravity is less than that on Earth and in which objects are weightless (Herranz et al., 2013), is another risk and is the focus of this thesis. Gravity affects all terrestrial objects, including the human body, and the human body has evolved in a manner that is dependent on gravity. Extended exposure to a microgravity environment alters the structures and the physiological processes that sustain human life, such as muscle tone and pressure and fluid dynamics (Amirova et al., 2021; Nelson et al., 2014).

Spaceflight Associated Neuro-ocular Syndrome

Spaceflight Associated Neuro-ocular Syndrome, also known as SANS, is a collection of alterations that can happen to the eye and to the visual system after long-duration exposure to microgravity (Mader et al., 2011). The clinical manifestations of SANS include unilateral or bilateral optic disc edema, globe flattening, choroidal folds, choroidal thickening, hyperopic refractive error shifts, and focal areas of ischemia in the retina, which can lead to decreases in visual acuity and visual field defects (Mader et al., 2011). Signs and symptoms of SANS can occur as a result both of long- and short-duration missions. Although most typically correct themselves after a return to Earth, some of these signs and symptoms can be permanent, especially after long-duration missions (Mader et al., 2011). There are substantial knowledge gaps in SANS literature, including the etiology of SANS and the pathophysiology of the ocular changes seen during and after spaceflight.

SANS occurs in both sexes but tends to occur more frequently in males than in females (Macias et al., 2020). Important work by Mader et al. (2011) studied seven astronauts, who had been on six-month long missions. Four of them experienced

symptomatic SANS in the form of a hyperopic shift. Two of them never developed symptoms but manifested signs of SANS, including optic disc edema, optic disc thickening, or flattening of the posterior globe. Of the seven astronauts, mild to moderate optic nerve head edema, which presented asymmetrically between the eyes, was noted in five subjects. This same study also surveyed 300 additional astronauts, who had been on long duration spaceflights, about in-flight vision changes. Approximately 52% of the surveyed astronauts did not report a decrease in near vision, which is often indicative of a SANS-related hyperopic shift. However, this study suggests that even if astronauts report no visual changes, it is still possible to present with ocular findings associated with SANS. Of the surveyed astronauts, it is possible that the 52% with no symptoms still had underlying structural alterations related to SANS.

Fundus photos and dilated fundus exams, magnetic resonance imaging (MRI), ultrasound, perimetry, and optical coherence tomography (OCT) are currently used to measure and to define SANS, pre-flight, in space, and post-flight (Lee et al., 2020). Of these, fundus photos, orbital ultrasound, and OCT are available on the ISS. Other available tests include visual acuity, tonometry, ophthalmoscopy, and Amsler grids (Lee et al., 2020). Fundus photos and ophthalmoscopy can help detect the presence of optic disc edema and cotton wool spots with high sensitivity and are also able to detect chorioretinal folds and peripapillary wrinkles (Lee et al., 2020; Mader et al., 2011). MRI scans can also identify optic disc edema and can indirectly show shifts in refractive error through the measurement of globe flattening, similar to the data collected with ocular ultrasound (Lee et al., 2020). An enlarged blind spot or a centrocecal scotoma on

perimetry may be a symptom of optic disc edema or posterior globe flattening (Lee et al., 2020). Tonometry performed during spaceflight can provide data on the normal intraocular pressure ranges astronauts experience and also can provide evidence for various theories of SANS pathophysiology.

OCT is the primary tool used on the ISS for the detection of the signs of SANS. OCT images structures in the posterior segment of the eye that are commonly altered by SANS, including the retina, choroid, and optic nerve head (Lee et al., 2020; Mader et al., 2019). Optic disc edema, retinal nerve fiber thickening, chorioretinal folds and peripapillary wrinkles, and cotton wool spots are common SANS-related pathologies that are readily detected on OCT (Lee et al., 2020). Mader and colleagues monitored ocular findings before, during, and after a six-month spaceflight to the ISS and demonstrated that OCT identified structural changes, such as mild choroidal thickening and an increased rim width of the optic nerve head, before changes were noted with ophthalmoscopy and fundus photography (Mader et al., 2017). Another advantage of OCT is that it provides objective quantification of these alterations, unlike ophthalmoscopy or fundus photography (Macias et al., 2020).

Although the mechanism of SANS has not been determined with certainty, it is likely a multifactorial disease process. There are several proposed mechanisms that may contribute to its pathophysiology (Figure 1).

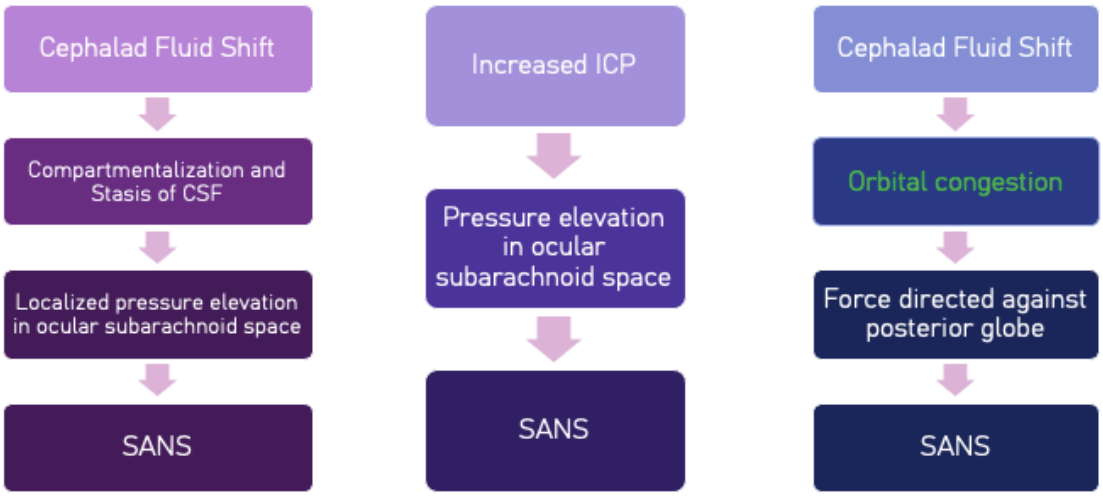

Figure 1. SANS Hypothesized Pathophysiologies Flow Chart

One of the proposed mechanisms is a cephalad (i.e., head-ward) fluid shift, promoting compartmentalization and stasis of cerebrospinal fluid (CSF) in the ocular subarachnoid space. This process can occur with or without increased intracranial pressure. Human bodies are acclimated to fluid pressure created by Earth's gravity, and removal of this pressure in microgravity environments allows for a head-ward fluid shift by changing intraorbital and intracranial CSF flow, as well as venous and lymphatics drainage (Macias et al., 2020; Mader et al., 2019; Mader et al., 2011). CSF is formed in the choroid plexus, flows into the subarachnoid space surrounding the brain, and drains out of the venous sinuses. In some mammals, including humans, up to 30% of CSF flows into the optic nerve subarachnoid space to drain into the lymphatics system (Morgan et al., 2016). The consistent drainage of CSF known to occur between the ocular and intracranial subarachnoid spaces is compressed in microgravity, leading to localized pressure elevation and sequestration of fluid within the optic nerve sheath and orbital subarachnoid space (Handel et al., 2021; Killer et al., 2007; Lee et al., 2020; Mader et al., 2019). Elevated pressure in vortex veins and in episcleral veins is also reported and can lead to decreased choroidal and aqueous humor drainage and can cause choroidal thickening and IOP elevation (Greenwald et al., 2021; Lee et al., 2020; Mader et al., 2019; Mader et al., 2011).

Shinojima et al. (2018) propose a related theory, that the microgravity environment in space allows the brain to shift slightly upward in addition to the cephalad fluid shift. This movement can be visualized as uplifted optic chiasms on MRI studies and could potentially pull posteriorly on the optic nerve and globe, contributing to

sequestration of CSF (Lee et al., 2020; Shinojima et al., 2018). It is theorized that optic nerve sheath distention, globe flattening, disc edema, and other structural changes that have been associated with SANS can be found as a result of CSF compartmentalization (Mader et al., 2019; Mader et al., 2017).

Increased intracranial pressure (ICP) caused by head-ward fluid shift in microgravity environments was an early hypothesis of the cause of SANS. This hypothesis centered on the fluids of the eye and brain, in particular CSF drainage from the ocular subarachnoid space. CSF production and drainage is thought to be determined by a balance between the high-pressure capillaries and low-pressure venules (Mader et al., 2011; Oreskovic & Klarica, 2010). The high-pressure capillaries have hyperosmolar plasma, which is osmotically driven towards the low-pressure venules with hypo-osmolar plasma (Mader et al., 2011). The microgravity environment can cause venous stasis and distention in these low-pressure CSF venules, creating a decrease in osmosis and therefore decreased CSF outflow and increased ICP (Mader et al., 2011). The increase in ICP is transmitted from the intracranial compartment to the ocular subarachnoid space, directing increased CSF pressure against the optic nerve (Lee et al., 2020; Mader et al., 2019; Mader et al., 2011).

ICP is hard to measure while in space and thus has not yet been attempted by NASA. However, one study was able to take direct measurements of ICP during parabolic flight through an Ommaya reservoir – a catheter that allows for insertion of needles into a CSF reservoir under the scalp and for the collection of uninterrupted and consecutive ICP measurements in microgravity (Lawley et al., 2017). The study found

that complete removal of gravity in parabolic flight did not cause pathological elevation of ICP, and that measured ICP was higher than that measured on Earth when standing yet lower than ICP measured in supine position. As humans spend most of our time upright, this increase is considered small. In addition, post-flight lumbar punctures range from normal to borderline high, a range of 21 to 28.5 cm of water (Lee et al., 2020). A small yet chronic increase in ICP is hypothesized to be a contributing element in SANS, but not independently sufficient to drive the pathophysiology of the syndrome. Another study conducted on dogs found that as CSF pressure increased, optic nerve subarachnoid space pressure, retrolaminar tissue pressure (translaminar pressure), and venous pulsation pressure also increased, suggesting a positive correlation between these pressures (Morgan et al., 2016).

On Earth, elevated ICP, such as in idiopathic intracranial hypertension (IIH), can present with symptoms of optic nerve sheath distention, globe flattening, choroidal and retinal folds, and optic disc edema (Friedman & Jacobson, 2004). However, these IIH symptoms can also be accompanied by neurological symptoms of chronic, severe headaches; pulse-synchronous tinnitus; diplopia; and transient visual obscurations, which are not seen in SANS (Lee et al., 2020; Mader et al., 2011). As astronauts typically do not report symptoms related to IIH, it is unlikely that the clinically significant disc edema seen in SANS is caused by elevated ICP alone (Mader et al., 2011). Moreover, the degree of optic disc swelling, sheath expansion, globe flattening, and choroidal folds are out of proportion to the slight increase in ICP found in astronauts (Lee et al., 2020; Mader et al., 2019; Mader et al., 2017). IIH patients present with substantially elevated ICP (range: 30

– 40 cm of water), much higher than the ranges found in astronauts (Lee et al., 2020). Although IIH could be a useful terrestrial analogue of SANS, due to several shared ocular signs, the numerous signs and symptoms that are present in IHH but not in SANS suggest that increased ICP is not the only factor at play in SANS and that the pathophysiology of IIH is not highly congruent with SANS.

The effect of a microgravity-induced head-ward fluid shift on the contents of the orbit has not yet been measured. However, orbital congestion has been proposed recently by Reilly et al. (2023) as a unifying mechanism for SANS. The microgravity environment would cause orbital edema, which in turn would push against the globe to elicit the features of SANS. That is, the orbital adipose tissue would become swollen and then apply an anteriorly directed force against the back of the eye, causing compression of the globe (Figure 2). The anatomy of the orbit contributes to the feasibility of this hypothesis. Orbital fat is surrounded by the orbital bones, which are rigid and non-flexible. This inflexible housing directs the force of the swollen soft-tissue contents of the orbit against the posterior globe and squeezes the optic nerve. With this theory, orbital congestion could manifest as globe flattening, hyperopic shifts, choroidal folds, decreased axial length, and optic disc edema, all of which have been described in SANS. To our knowledge, proptosis has not been documented in astronauts, but it is plausible that it occurs to a small degree in SANS (Reilly et al., 2023).

As proof of concept for this orbital congestion theory, Reilly et al. constructed a geometric model using COMSOL Multiphysics, a computer-simulation platform, to replicate orbital congestion. The model tested for potential of edematous orbital adipose

tissue to affect axial length, posterior radius of curvature of the globe (ROC), peripapillary arc length, and proptosis. Model predictions also included the potential effects of ICP and EOM tension. Axial length, posterior ROC, peripapillary choroidal arc length, and proptosis were found to be strongly dependent on orbital fat swelling but only weakly influenced by ICP (Reilly et al., 2023). Notably, axial length and peripapillary choroidal arc length decreased, suggesting flattening of the globe and decreased choroidal tension. Posterior ROC and proptosis simultaneously increased, which also suggested that the force of the orbital fat was pushing the globe anteriorly. These findings in the model correspond with physical signs and symptoms found post-spaceflight in astronauts. The next step in this line of research is to find a suitable terrestrial ocular condition to further explore this orbital-congestion hypothesis. This thesis focuses on the ability of orbital imaging to quantity orbital swelling in one such condition, thyroid eye disease.

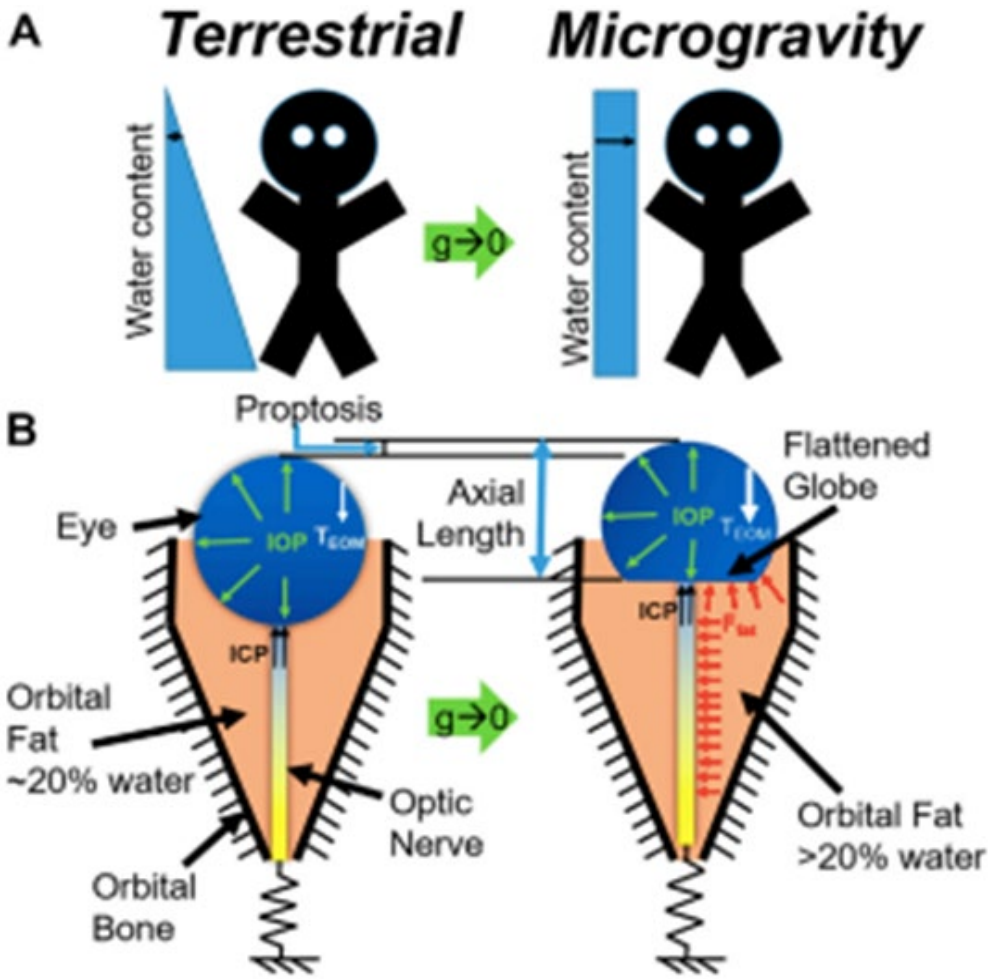

(A) Representation of microgravity-induced fluid shift and (B) corresponding changes in the eye and in the orbit. From Reilly et al., 2023.

Figure 2. Orbital Congestion

There are no established treatments for SANS. As a limited therapy, NASA currently uses plus-powered spectacles to attempt to counteract hyperopic shifts during and after spaceflights. The best therapy for SANS, however, is to prevent it from occurring – an active line of research in the space community. The creation of artificial gravity is a proposed countermeasure to SANS. As introduced above, the loss of gravity is believed to substantially contribute to the development of SANS. Thus, the reestablishment of a gravity field during spaceflight might be efficacious in preventing SANS. One method of creating "artificial" gravity is through centrifugation. This method of gravity creation allows for variation of the strength and the direction of the force, potentially mimicking a terrestrial environment (Anderson et al., 2018). Cardiovascular performance metrics under centrifugal gravity are similar to terrestrial values, but IOP remains relatively elevated (Anderson et al., 2018). It is important to note that these data were collected on Earth, so the terrestrial gravity-inertial force that aids in self-orientation might have increased IOP. An experiment on artificial gravity done in space would be complicated, but it would fully allow for the testing of true artificial gravity against the effects of microgravity on the body.

Inducing lower-body negative pressure may be a second counteractant to SANS. Lower-body negative pressure is often utilized in experiments as simulation of gravitational stress. The subject is partially inserted into a tube from the waist down, and air is sucked out of the tube. The resultant negative pressure causes the movement of fluid and blood down toward the legs and away from the head, decreasing ICP (Marshall-Goebel et al., 2017; Watkins et al., 2017). Head-down tilt was combined with this

technique to assess its efficacy in a setting that imitated a microgravity environment. Head-down tilt was found to increase internal jugular vein cross-sectional area and ICP, as expected. When head-down tilt was combined with lower-body negative pressure, however, the jugular vein cross-sectional area and ICP decreased (Watkins et al., 2017). These results suggest that lower-body negative pressure was able to mitigate some of the effects of simulated microgravity (Marshall-Goebel et al., 2017; Watkins et al., 2017). Magnitude of the negative pressure matters, as relatively low levels of lower-body negative pressure might not be able to reduce ICP during long exposures to simulated microgravity (Marshall-Goebel et al., 2017). Further studies are necessary understand whether lower-body negative pressure is effective in space against actual SANS, but it is a promising treatment.

If long-duration space travel is to be a reality, additional therapies may be needed to manage the structural alterations caused by SANS. Before such therapies can be developed, however, the pathophysiology of the syndrome must be elucidated. Before the pathophysiology of SANS can be established, tools must be developed to measure in-flight ocular health and intracranial and intraocular pressure. There are limitations to the research that can be done while in space, such as a set research schedule on the ISS, limited storage of equipment, and a small population of research subjects; therefore, a ground-based analogue for SANS is needed to spur future studies that can develop therapies to manage the condition. The research of this thesis is an initial step toward developing a terrestrial analogue to fill this need.

Terrestrial Analogue of SANS

There are several non-disease-based models that have been used to imitate SANS on Earth. Head-down tilt may most closely approximate microgravity by inducing a chronic head-ward fluid shift (Stenger et al., 2017). This spaceflight analog has been used to study both the possible mechanism of SANS as well as to evaluate treatment methods, such as lower-body negative pressure devices (Watkins et al., 2017). One study by Laurie and colleagues assessed a cohort of 11 healthy subjects before, during, and after a strict head-down tilt at 6°, as well as a cohort of 20 astronauts before and during spaceflight (Laurie et al., 2020). More optic disc edema developed in head-down-tilt subjects than in the astronaut cohort. Contrarily, choroidal thickness increased in spaceflight but not in head-down tilt. However, in a later study, in which OCT was performed with head-down tilt, chorioretinal folds developed in 6 out of 24 subjects (Laurie et al., 2021). Although it is not a perfectly equivalent analog, head-down tilt allows for more testing capabilities than what is available during spaceflight due to time, space, and subject limitations. Other body positioning studies that tested subjects in supine versus prone posture have shown that axial length and corneal thickness are greater in prone posture than in supine posture, but supine posture leads to greater choroidal volume (Anderson et al., 2017). These experiments mimicked the microgravity effects of space on the human body and show that induced fluid shifts in the body can have measurable effects on the structure of the eye.

Parabolic flight is a second important analog to zero gravity in space flight, as it can elicit a microgravity environment that is similar to, and more easily obtained than,

space travel. However, this model is limited in time, with free fall occurring for only about 20-25 seconds sequentially (Pletser et al., 2009). One study measured axial length, lens thickness, anterior chamber depth, corneal thickness, and intraocular pressure and collected OCT images from subjects during parabolic flight (Anderson et al., 2016). There was a small yet significant decrease in anterior chamber depth as well as an increase in choroidal area, compared to seated and supine postures. These changes are consistent with the removal of normal hydrostatic gradients seen on Earth, elimination of which may cause venous congestion and stasis. Head-ward fluid shifts found in microgravity raise ocular venous pressure (episcleral, vortex, and choroidal) and induce choroidal expansion, which can in turn influence IOP. Measurements of IOP during spaceflight normalize with time, suggesting that another volume compartment of the eye compensates for the increase in choroidal volume by decreasing in size – likely the anterior chamber (Mader et al., 2019).

Although head-down tilt and parabolic flight can be performed without traveling into low-Earth orbit, chronic disease processes that are mechanistically similar to SANS may be optimal real-world models of its pathophysiology. Thyroid eye disease (TED) is a potential terrestrial analogue for SANS because its signs and symptoms closely match those of SANS (Table 1) (Reilly et al., 2023).

TED Possible Presentations	SANS Possible Presentations
Optic disc edema	Optic disc edema
Orbital edema	Orbital edema
Choroidal folds	Choroidal folds
Changes in refractive error	Hyperopic refractive error shifts
Proptosis	Choroidal thickening
Lid edema	Focal areas of ischemia in the retina
Retracted eyelids	
Erythema	

Table 1. Comparison of TED and SANS Known Presentations

TED is a common manifestation of Graves disease, where the thyroid gland is overactive due to the production of self-antibodies that imitate thyroid stimulating hormone (TSH) and overstimulate the secretion of thyroid hormones (Debnam et al., 2021; Lacheta et al., 2019). The autoantibodies created in Graves disease also target self-tissue and contribute to the activation of orbital fibroblasts and preadipocytes, which promote the activity of inflammatory mediators, such as cytokines and mononuclear cells, in the orbital adipose tissue and in the fibrous tissue of the extraocular muscles (Lacheta et al., 2019). These cytokines lead to synthesis of glycosaminoglycans (GAGS), such as hyaluronic acid, which draw fluid into the retrobulbar tissue of the orbit, causing edema (Debnam et al., 2021; Lacheta et al., 2019). In addition, adipogenesis occurs and intensifies the accumulation of orbital fat. Increased water, from inflammation, and increased adipose tissue in the orbit exert pressure against the globe, leading to ocular manifestations of the disease. Specifically, Graves orbitopathy can present with varying severities of proptosis, edema, retracted eyelids, erythema, disc edema, choroidal folds, and changes in refractive error (Chandrasekaran et al., 2006). Many of these manifestations are similar to SANS. Moreover, TED is characterized by edema of the orbital adipose tissue pushing on the globe, which is consistent with the orbital congestion hypothesis for the mechanism behind SANS (Reilly et al., 2023). Thus, TED is a promising terrestrial analog.

Measurement of Orbital Fat

There are multiple strategies for imaging of the orbit that can be instrumental in the diagnosis and treatment of ocular disease. These include computed tomography (CT), magnetic resonance imaging (MRI) scans, and orbital ultrasound. MRI is specifically

useful in the detection of adipose tissue through fat suppression techniques (Delfaut et al., 1999). One specific group of MRI sequences that use fat suppression, quantitative Dixon or q-Dixon, has proven to be an effective method of quantifying fat-water fraction measurements. Q-Dixon sequencing consists of several acquisitions that allow for the separation of water and fat signals by combining or subtracting signals from the acquired images (de Kerviler et al., 1998). In general, q-Dixon sequencing has many uses, including research, therapeutic testing, and diagnostics.

The q-Dixon technique was developed in 1984 by W Thomas Dixon, who realized the potential for an imaging method that utilized the chemical shift frequencies of water and fat measured through MRI (de Kerviler et al., 1998). One measurement is taken while the signals of water and fat are aligned and facing the same way – "in-phase" – while another is taken while the water and fat signals are facing opposite each other – "out-of-phase." Water and fat signals summate when measured together during the "in-phase" segment, but they negate each other when they are measured "out of phase." This dichotomy allows for the calculation of fat and water percentages (de Kerviler et al., 1998; Zhai et al., 2021).

We use the q-Dixon technique in this study because it has some important advantages over other potential methods of fat suppression and fat-water fractioning. Other methods of fat suppression are susceptible to magnetic field heterogeneity, to misregistration artifacts during the imaging process, and to low-strength magnets (Delfaut et al., 1999). The q-Dixon method suppresses fat signaling uniformly and generates fewer artifacts during the scan than other methods. It also is easily combined

with other techniques (de Kerviler et al., 1998). Some drawbacks of the q-Dixon technique include a long sequencing duration and the requirement for post-processing to get the precise measurements of fat and water. Overall, the benefits of this technique outweigh its drawbacks.

Two recent studies have tested how q-Dixon techniques compared against conventional methods of imaging for the diagnosis of thyroid eye disease. Important work by Alexis Ollitrault et al. prospectively tested q-Dixon-T2-weighted imaging (WI) compared to T1, T2, and fat suppressed T2 weighted MR imaging in patients with TED (Ollitrault et al., 2021). Another study by Lu Chen et al. retrospectively examined the two-point q-Dixon-T2-WI technique against conventional fat-saturation (CHESS) T2-WI in patients with TED (Chen et al., 2021). Ollitrault et al. found that q-Dixon-T2WI was 100% sensitive for TED and that the conventional T1, T2, and T2WI sequences were only 94% sensitive. Q-Dixon-T2WI also had higher specificity than the conventional set. In addition, significantly fewer non-motion artifacts were found in the q-Dixon-T2WI scan. Limitations of this study included a single study center and high variability q-Dixon MRI sequences, which can affect reproducibility of study results. Nevertheless, the results of the Ollitrault study confirm that q-Dixon-T2WI imaging is the better method for imaging of TED over conventional imaging. Chen et al. produced similar results. The q-Dixon-T2WI technique showed significantly better fat suppression uniformity, higher image quality, and higher extraocular muscle (EOM) signal intensity ratio than traditional techniques. Both studies show this method can indeed be helpful in confirming the

diagnosis of TED or in assessing the extent of inflammation and enlargement of orbital fat.

While q-Dixon is valuable in clinical diagnosis, it also has utility for research on the orbits. Kaichi et al. used FSE-IDEAL, a novel 3-point q-Dixon sequence, to test the effectiveness of methylprednisolone pulse therapy as a treatment option for TED (Kaichi et al., 2016). They found that methylprednisolone pulse therapy was successful at reducing the orbital water volume, but there was no significant reduction in orbital fat volume between pre and post treatment. Therefore, the therapy was found to be useful in patients with TED that had a high water content. Although the study had a small sample size, and although the studied MRI sequence itself may vary from vendor to vendor, it shows how q-Dixon methods of fat-water fractioning can be effective in research.

Normal orbital fat fraction percentages in the orbit have been reported to range between 72.5-85% fat, but this value may fluctuate with the health of the orbit (Kaichi et al., 2016; Kaichi et al., 2019). Q-Dixon imaging will help take precise and accurate measurements of the orbital fat content in patients with TED, and validating this beforehand with orbital phantom experimentation strengthens the use of this imaging modality. ImageJ, an image processing software we use to analyze the acquired q-Dixon MRI scans, allows for specific designation of regions of interest to focus on in these scans. This approach enables additional precise measurements of retrobulbar fat and gives a direct comparison to the orbital congestion that we propose occurs in space and leads to SANS. Imaging of TED subjects before treatment mimics the proposed changes of increased orbital congestion astronauts go through in the development of SANS. By

acquiring repeat MR images after TED decompression surgery or medical decompression, this simulates the astronauts at baseline before increased orbital congestion and the occurrence of SANS. In this thesis, we evaluate the ability of q-Dixon imaging to quantify fat-water percentages of TED patient, who has not yet undergone medical treatment, in order to begin to assess TED as a ground-based analog to SANS.

Purpose

Humans have not yet traveled to a different planet. To do so, we first must establish the mechanisms of SANS, and we must learn how to counteract its deleterious effects on the eye and on vision. These goals are urgent because missions to Mars are actively being planned. One hypothesized mechanism is orbital congestion during microgravity that applies a force to the posterior globe to cause optic disc edema, hyperopic shifts, cotton-wool spots, choroidal folds and choroidal thickening, and optic nerve sheath distension. This is a unifying hypothesis that covers all reported features of SANS. However, the critical gap is developing an appropriate terrestrial analogue and demonstrating a method to quantify changes in orbital fat-fraction that is accurate and reliable. In this thesis, we evaluate the ability of q-Dixon imaging to quantify fat-water percentages of the orbit in TED. Promising research has already been performed concerning ways to study SANS while on Earth, yet we believe even more can be learned about SANS by studying TED.

The overarching aim of this thesis is to contribute to the scientific community's ability to study the changes that occur in the orbit of the human skull in microgravity environments. Specifically, this study evaluates new methodology to assess the fat

fraction of the orbital contents in one potential terrestrial analogue for microgravity environments, TED. As the next step in establishing this disease as a terrestrial analogue for the proposed mechanism of SANS, the purpose of this thesis is to test the ability of the previously described MRI sequence to assess orbital phantom models of varying fat-water percentages. We will use the same technology to quantify fat fractions in the orbits of one patient with TED.

Chapter 2. Methods

This study represents initial work to determine whether TED is a suitable ground-based analog to SANS. Preliminary experiments validated the ability of a q-Dixon Multi-Echo Chemical Shift Encoded MRI at 3 Tesla to determine the percentages of orbital fat and water. First, orbital phantoms, which contained varying ratios of fat and water, were imaged to test the range and accuracy of the MRI sequence. Then, the initial subject with TED was enrolled. Baseline MRI imaging was conducted and ImageJ software was used to determine specific ratios of retrobulbar fat and water in the baseline MRI scans.

Phantom Construction

In order to test the accuracy of, the precision of, and the smallest measurable increment of the MRI sequence, we first built several phantom models designed to simulate ranges of fat-water percentages that may be present in the orbit. Two sets of phantoms were constructed at The Ohio State University (OSU). The first focused on both extremes – small fat percentages and large fat percentages (0%, 0.5%, 1%, 80%, 81%, 100%). The second explored a wide range of percentages (0%, 3%, 6%, 9%, 70%, 75%, 80%, 85%, 90%).

The phantoms were constructed in 50 mL scintillation vials, and appropriate amounts of fat and water were mixed together to create the respective fractions (Table 1).

Peanut oil was used as the fat component, as its nuclear magnetic resonance spectrum resembles the spectrum of triglycerides in adipose tissue (Hines et al., 2009). Deionized water, sodium dodecyl (6200 mg; surfactant), sodium chloride (1260mg), sodium azide (122mg), and gadobenate dimeglumine (145.6mL) were used to create the water solution and to promote homogenization.

Fat percentage	Peanut oil (mL)	Water solution (mL)
TRIAL 1		
0% fat	0.00	25.00
0.5% fat	0.13	24.88
1% fat	0.25	24.75
80% fat	20.00	5.00
81% fat	20.25	4.75
100% fat	25.00	0.00
TRIAL 2		
0% fat	0.00	25.00
3% fat	0.75	24.25
6% fat	1.50	23.50
9% fat	2.25	22.75
70% fat	17.50	7.50
75% fat	18.75	6.25
80% fat	20.00	5.00
85% fat	21.25	3.75
90% fat	22.50	2.50

Table 2. Fat-water Fractions of the Model Phantoms

The deionized water was placed in a 500 mL beaker overtop of a hotplate at 95° C with a stir bar to aid in dissolution. The other components of the water solution and 2% weight/volume agar were added over heat and stirred until the mixture was dissolved. When the solution was well mixed and clear, the water solution was pipetted in the determined amounts into the scintillation vials with the appropriate peanut oil amounts. The vials were hand inverted until the phantoms were homogenized. They were then placed into a refrigerator at 4° C for one hour to promote setting and solidification.

Although the phantoms made at OSU initially set (Figure 3A), their fat and water components separated within 2 hours of setting, precluding imaging. Therefore, custom commercial phantoms were ordered from Calimetrix (Madison, Wisconsin). These phantoms were made with a homogenizer to completely emulsify the components (Figure 3B). The fat percentages of the custom commercial phantoms were 0%, 5%, 10%, 15%, 20%, 30%, 40%, 50%, 60%, 70%, 80%, 85%, 90%, and 100% (Figure 3B-C).

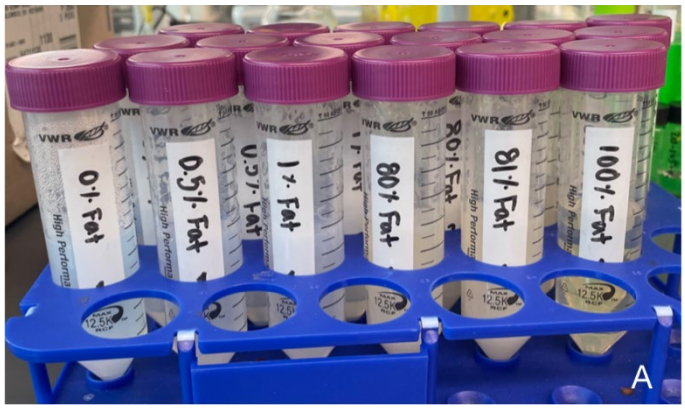

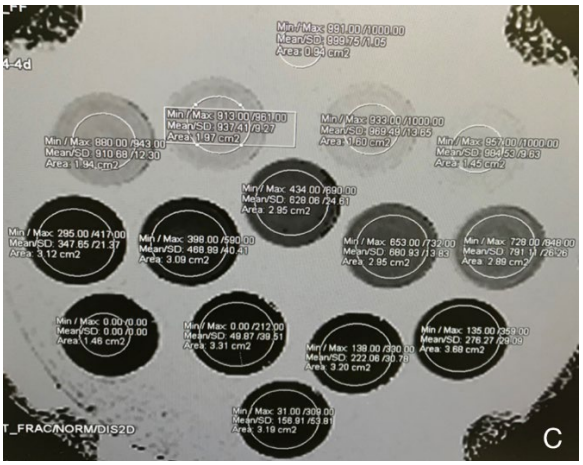

A - First orbital phantoms, in which the fat-water compound initially set, but later separated. B - Custom-made orbital phantom, which contained a homogenized fat-water compound. C - Representational outcome of fat-water fraction MRI imaging of the phantoms.

Figure 3. Examples of Fat-Water Phantoms

Sequence Validation

MRI imaging of the custom commercial phantoms was performed by the Department of Radiology in the College of Medicine at OSU. Specifically, a q-Dixon Multi-Echo Chemical Shift Encoded MRI at 3 Tesla with a standard 32-channel head coil array quantified the fat-water ratios of the phantoms. Images of the phantoms were acquired in triplicate in three orientations to accomplish two goals: 1) to evaluate test-retest reliability of the sequence and 2) to test the accuracy of the sequence, in comparison to the true fat-water ratios of the phantoms. Figure 4 contains the three orientations of the phantoms. In Position 1, the phantoms were placed in a head-to-foot direction, which is consistent with the orientation of human subjects in the magnet bore. In Position 2, the phantoms were placed oblique to the scanner. In Position 3, the phantoms remained oblique to the scanner but were raised on a foam stand and were pointed downward.

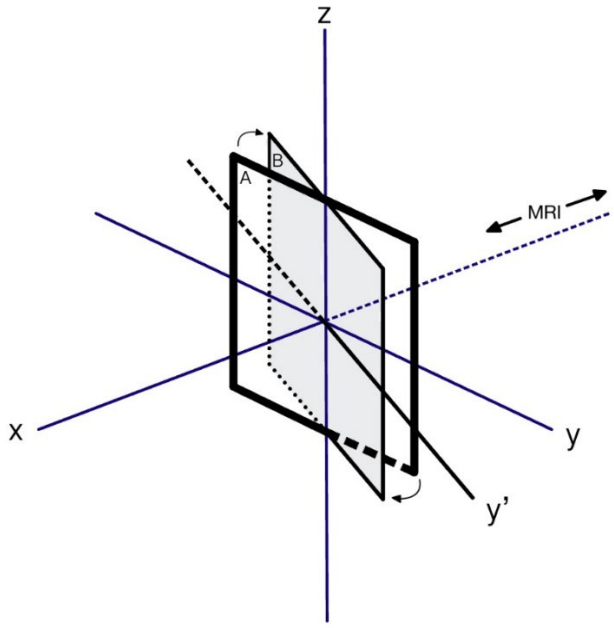

Figure 4 shows the x-, y-, and z-axes, with y' notating the rotated y-axis. Plane A is parallel to the y-axis, and plane B is rotated from that around the z-axis and is parallel to the y'-axis. The length of the MRI machine is located along the x-axis, with plane A representing the front of the machine. The orientation of the phantoms in Position 1 is portrayed by plane A pointing along the x-axis into the MRI machine. Position 2 is similar to the first, yet it is rotated and inserted obliquely to the scanner, exemplified by plane B. Position 3 is similarly rotated obliquely to plane B, but also pointed downwards along the z-axis.

Figure 4. Orientation of Phantom Models in the Scanner

Human Experiments

Once validation of the MRI sequence was complete, the human-based arm of the study could begin. This study was granted approval through the OSU Biomedical Institutional Review Board, and all participants provided informed consent before enrolling.

Participants

This study aims to eventually recruit a total of 50 subjects (N = 50) into two cohorts, a treatment cohort and a control cohort. The treatment group will comprise 10 patients (n = 10) with TED treated with surgical decompression, 10 patients (n = 10) with TED treated with medical decompression (teprotumumab), and 5 patients (n = 5) with carotid-cavernous fistula. Twenty-five healthy subjects (n = 25) will be recruited as age- and sex-matched controls. All subjects will be recruited from community ophthalmology and optometry practices.

Subject enrollment is in its earliest stage. Thus, only the preliminary data from the first subject in the treatment group are reported in this thesis.

MRI Imaging and Data Collection

Triplicate MRI scans were performed on the head and orbits using the q-Dixon Multi-Echo Chemical Shift Encoded MRI sequence to measure fat and water percentages of retrobulbar fat. Initial pre-treatment images were taken in the axial plane, with the

subject lying in the supine position. Head stabilization was not utilized during MR imaging.

MR Image Processing

The MR images of the first untreated subject with TED in the treatment cohort were acquired in triplicate. Each scan focused on the brain and orbits and comprised 48 slices. Initial measurement errors in computed values overestimating true fat values at high- and low-fat fractions were corrected using a customized off-line processing algorithm.

The corrected scans were uploaded to ImageJ (Laboratory for Optical and Computational Instrumentation; University of Wisconsin, Madison), an image processing software, and were combined to stacks, which allowed the user to scroll through them. Then, selected regions of interest (ROI) were identified and outlined targeting retrobulbar fat, which is represented as a light gray color, of one orbit at a time using the Wand (tracing) tool (Figure 5). Specifically, with this tool, the fat selection was defined voxel by voxel based on voxel intensity. A large-intensity threshold value, 10, was initially used to select the general orbital area. This threshold was then decreased in value (to 1-2) to specifically hone in on orbital fat and make the ROI more precise (Figure 6). The smaller the threshold number, the fewer voxels would be selected at a time – dependent on how close the gray scale value of each voxel is to neighboring voxels. Once the region of orbital fat was identified and outlined, the percentage of fat compared to water was measured in the region of interest outlined area by selecting “Analyze” and then

"Measure." This tool gives the mean gray value of all of the voxels in the selected region reported in optical density, with higher numbers corresponding to higher fat percentages.

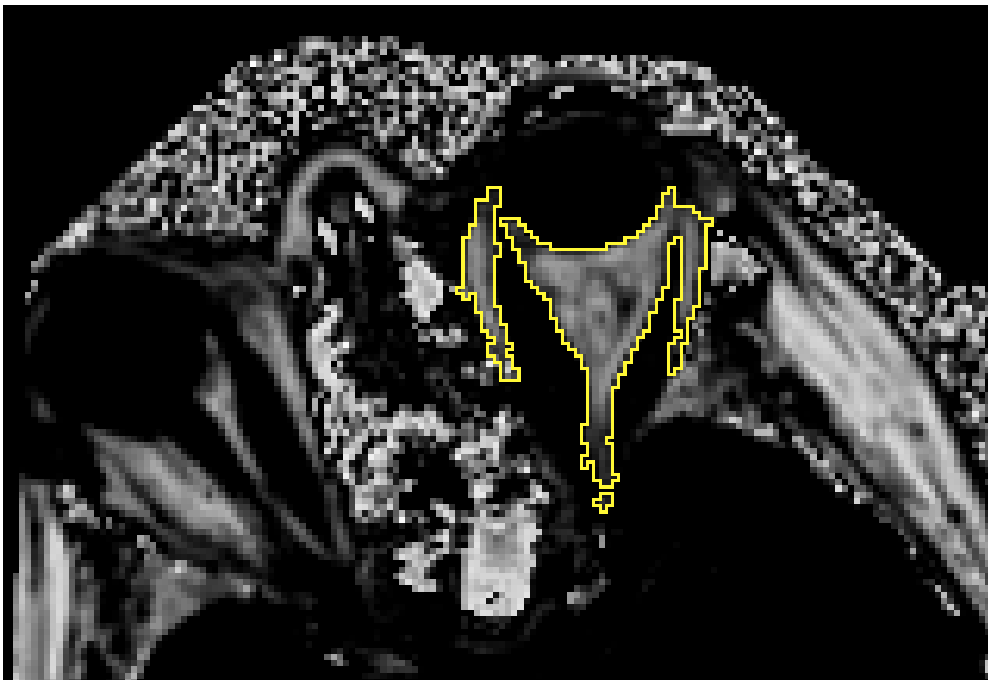

The subject was imaged in the axial plane focusing on the brain and orbit. Retrobulbar fat is highlighted using the Wand (tracing) tool on the subjects' left eye. When measured, the mean gray value of only the selected voxels in this slice of the scan is assessed.

Figure 5. Example of Retrobulbar Fat Region of Interest Measured

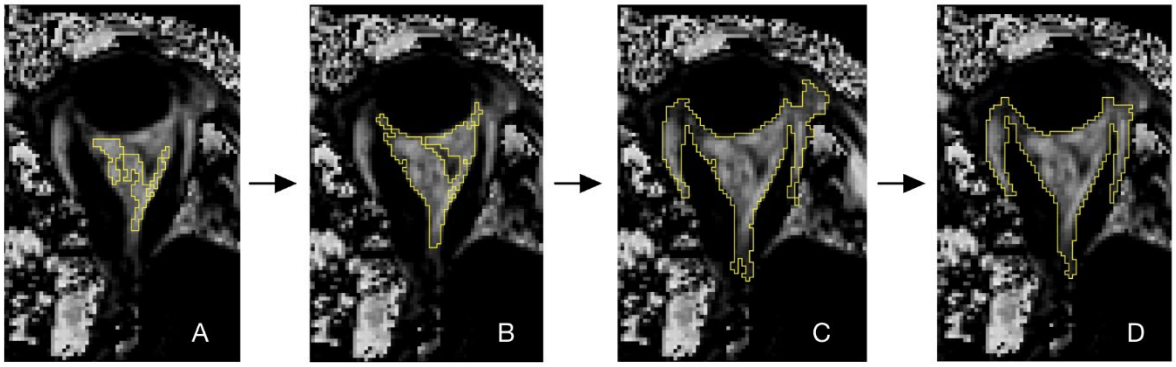

A - The first selection using a large threshold number; B - Selecting more voxels using the same large threshold; C - Final selection with the large threshold number; D - Using a small threshold number to hone in precisely on retrobulbar fat.

Figure 6. Example Region of Interest Selection Process

Statistical Analysis

Phantom Experiments

MR imaging results for the phantoms were obtained and processed to generate specific fat-water percentages. The positions were analyzed for test-retest repeatability and accuracy compared to true values. Accuracy in each position was analyzed through calculation of absolute average deviation from true fat values, deviation range, and coefficient of variation (COV). Repeated-measures (RM) analysis of variance (ANOVA) was performed for all three positions to gauge variability of results based on positioning and repeatability of measurements. Accuracy and repeatability were also analyzed by plotting the measured fat value of the triplicate scans in each position against the true fat values to determine the linear relationship.

Human Experiments

Preliminary results of imaging and ImageJ analysis of one subject with untreated TED were acquired and images were processed in ImageJ as described above. This first subject was initially scheduled for repeat imaging post-treatment, but was not able to complete the study due to medical reasons, so only pre-treatment images were processed. Measured fat-fraction values were then weighted by volume of the corresponding region of interest. Specifically, for a given MRI slice, orbital fat volume for the selected region of interest was divided by the total orbital fat volume measured for that orbit. This value was then multiplied by the fat-water fraction in the same slice to give the volume-weighted fat-fraction profile of the slice. Finally, the volume-weighted fat-water fraction of each slice in a given sequence were summed to provide the average fat-water fraction of the orbit.

Variability of the volume-weighted fat-water fraction per slice within each orbit was quantified using standard deviation and coefficient of variation. RM ANOVA tested differences in fat-water fraction and orbital fat volume between each of the three scans in each orbit. Then, volume and average fat-fraction measurements of the right and left orbits were compared using a paired t-test. Lastly, the distribution of slice volume and fat-fraction percentages for the right and left orbits was plotted by slice number for each of the three scans to view the placement of orbital fat slice by slice.

Chapter 3. Results

Phantom Model Results

MRI-measured fat-water fraction ratios of the custom-made phantom models were assessed in three positions for test-retest errors and for accuracy compared to true values. Each position had good accuracy (Table 3), and there was no difference in accuracy ($p = 0.30$, RM ANOVA) between the three positions (Figure 7). There was a strong linear association between measured and true fat values in all three positions ($R^2 = 0.9978$, Figure 8).

	Absolute Average Deviation from True Fat Fraction ± Standard Deviation	Deviation Range	Coefficient of Variation
Position 1	1.4% ± 0.9%	0% to 3.1%	0.01
Position 2	1.3% ± 0.8%	0.1% to 2.9%	0.05
Position 3	1.8% ± 1.5%	0% to 5.2%	0.06

Accuracy of fat-water MRI imaging of the custom-made orbital phantoms positioned in three different orientations. Values are absolute differences between measured fat percentage and true fat percentage.

Table 3. Accuracy of Phantoms in Three Orientations

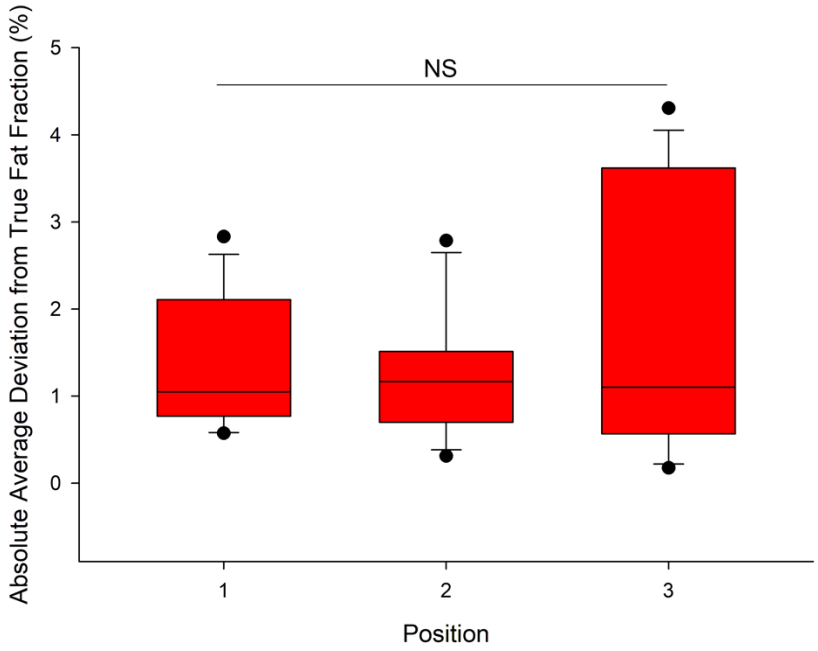

Each box represents the interquartile range for each phantom position, and the internal lines are the median absolute average deviation. The whiskers represent the 90th and 10th percentiles, with circles representing outlying values. NS is not significant, analysis of variance.

Figure 7. Absolute Average Deviation from True Fat Fraction Values

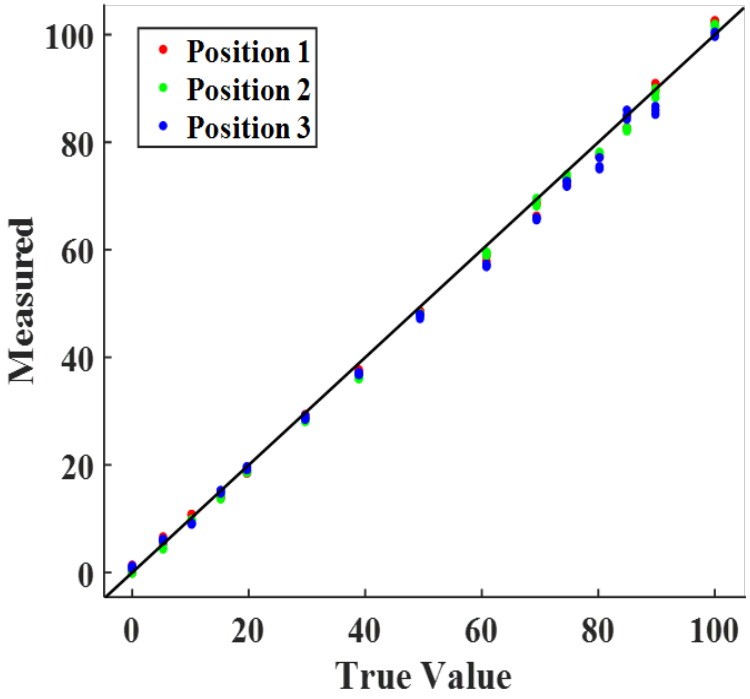

Accuracy of fat-water MRI imaging of the custom-made orbital phantoms positioned in three different orientations with scans repeated three times. Values are percentage fat.

Figure 8. Measured versus True Fat Value

Preliminary Human Subject Results

The repeatability of the triplicate scans of the first treatment subject, a 76-year-old Caucasian woman diagnosed with TED and scheduled to be treated with teprotumumab, were analyzed for orbital fat volume and for fat fraction in the orbit. For the right orbit (Figure 9), there was a statistically significant difference ($p = 0.04$, RM ANOVA) in fat fraction between the first scan and the third scan. There were no statistically significant differences ($p > 0.05$) between first scan and the second or between the second scan and the third scan. For the left orbit (Figure 10), there was a statistically significant difference ($p = 0.006$; RM ANOVA on ranks) in fat fraction measured between the second scan and the third scan. There were no statistically significant differences ($p > 0.05$) between the first scan and the second scan or between the first scan and the third scan. Both in the right orbit (Table 4) and in the left orbit (Table 5), the COV was approximately doubled for orbital fat volume compared to fat fraction.

There were no statistically significant differences between the orbits both for volume ($p = 0.08$, paired t-test; Figure 11) and for fat fraction ($p = 0.27$; Figure 12).

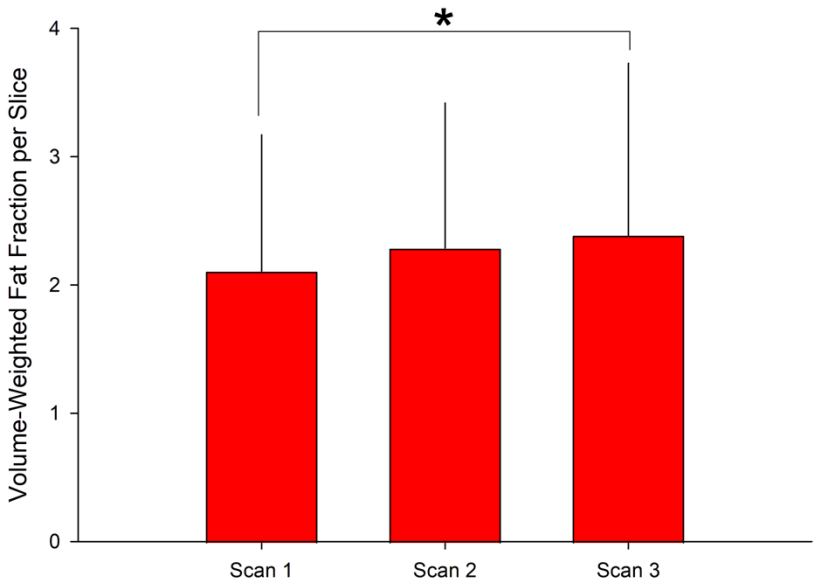

Average ± standard deviation volume-weighted fat fraction per slice for scans 1, 2, and 3 in the right orbit. *p < 0.05, repeated-measure analysis of variance.

Figure 9. Right Orbit Fat Fraction by Scan

	OD		
	Mean	SD	COV
Orbital Volume (voxels)	8074.77	1106.39	0.14
Orbital Fat Fraction (%)	42.97	2.68	0.06

Comparison of orbital fat volume and fat fraction for the right orbit.

Table 4. Right Orbit Fat Fraction and Orbital Fat Volume Measured

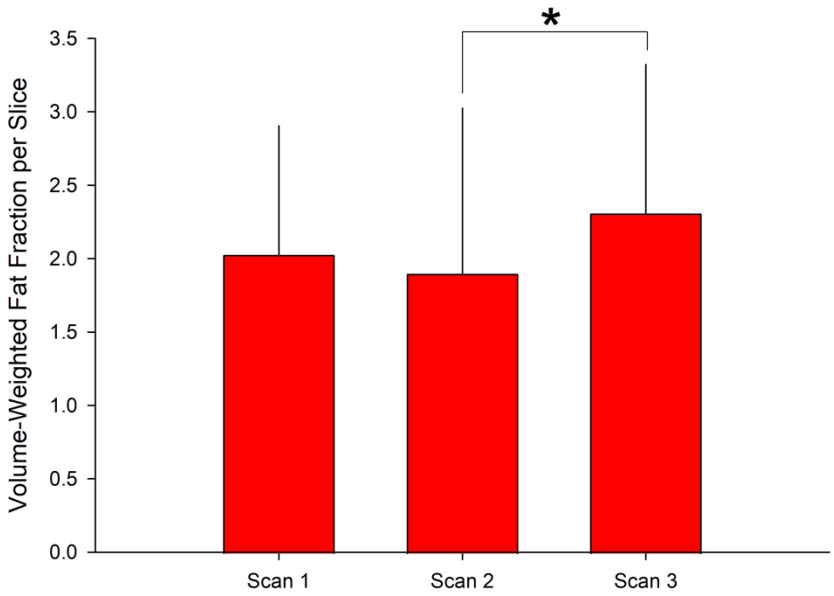

Average ± standard deviation volume-weighted fat fraction per slice for scans 1, 2, and 3 in the left orbit. *p < 0.05, repeated-measure analysis of variance on ranks.

Figure 10. Left Orbit Fat Fraction by Scan

OS			
	Mean	SD	COV
Orbital Volume (voxels)	8988.60	1152.51	0.13
Orbital Fat Fraction (%)	42.08	3.04	0.07

Comparison of orbital fat volume and fat fraction for the left orbit.

Table 5. Left Orbit Fat Fraction and Orbital Fat Volume Measured

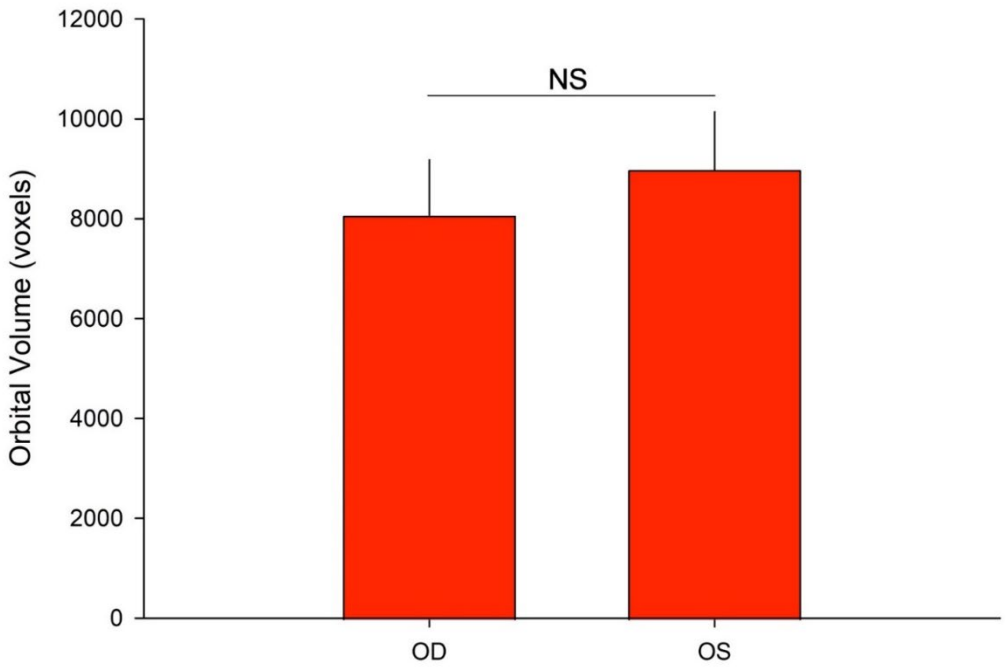

Average ± standard deviation orbital fat volume of the right and left orbits. NS is not significant, paired t-test.

Figure 11. Right Orbit vs Left Orbit Fat Volume

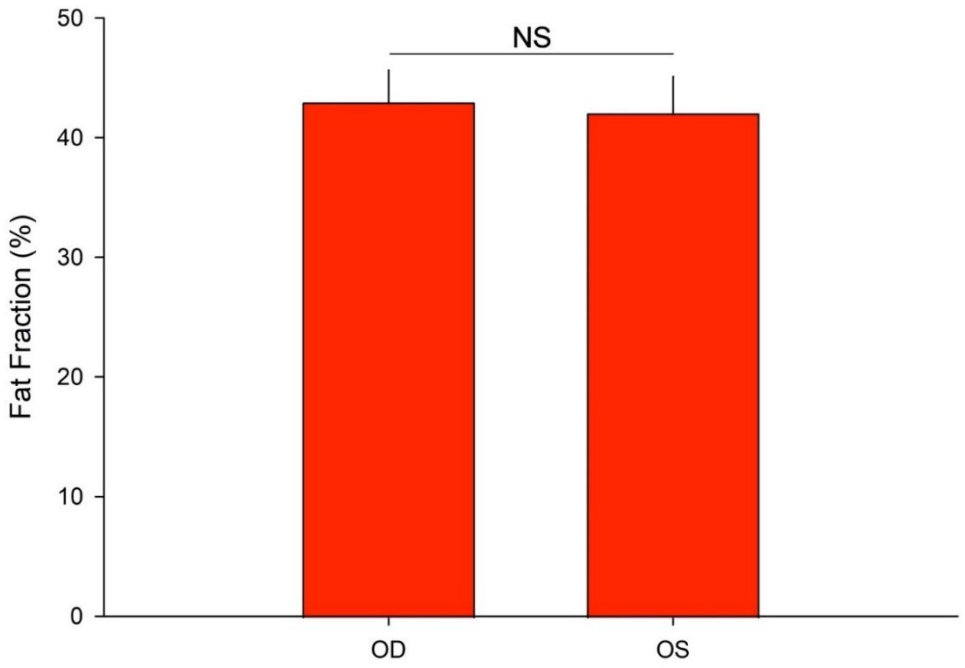

Average ± standard deviation fat fraction of the right and left orbits. NS is not significant, paired t-test.

Figure 12. Right Orbit vs Left Orbit Fat Fraction

Assessment of fat volume as a function of MRI slice revealed a roughly biphasic curve, both in the right orbit (Figure 13) and in the left orbit (Figure 14). Alignment of fat volume varied between the scans in both orbits but especially in the left, where the first group of scans was dramatically offset from the second and third groups. In the right orbit, fat fraction was the highest toward the bottom (low slice numbers) of the orbit and fluctuated throughout the scan, presumably higher away from the extraocular muscles and the optic nerve. This was the same general pattern in the left orbit, with peaks around the bottom and top (high slice numbers) of the orbit.

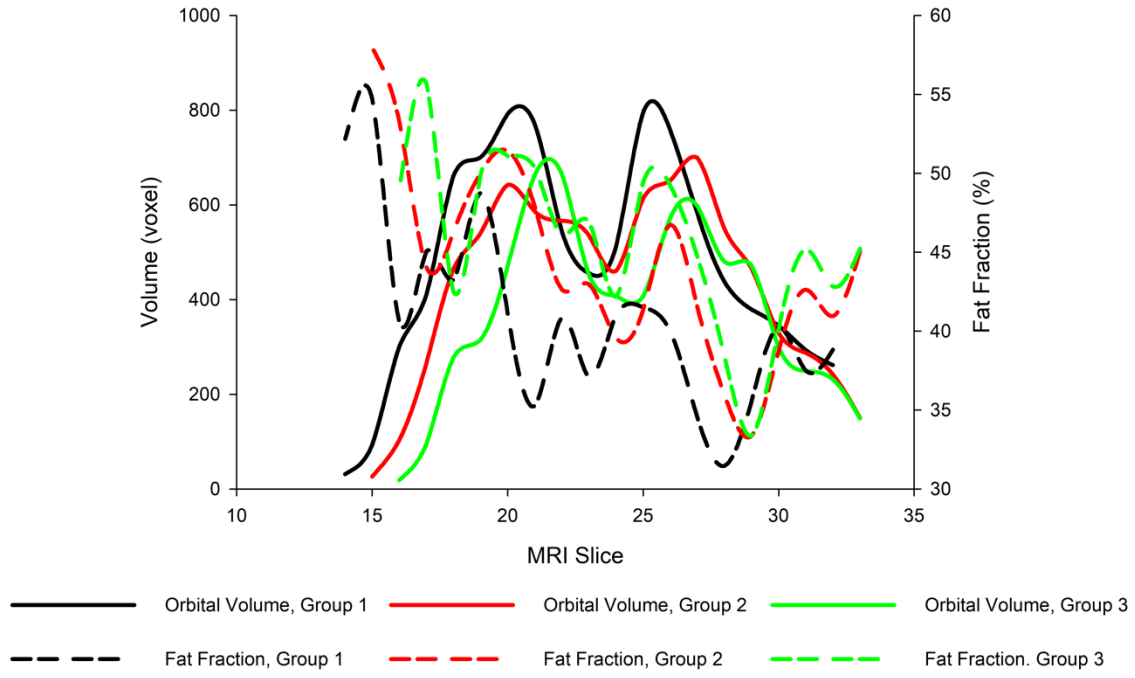

Average fat fraction and orbital fat volume per slice measured for the three MRI scans of the right orbit.

Figure 13. Right Orbit Fat Fraction Profile

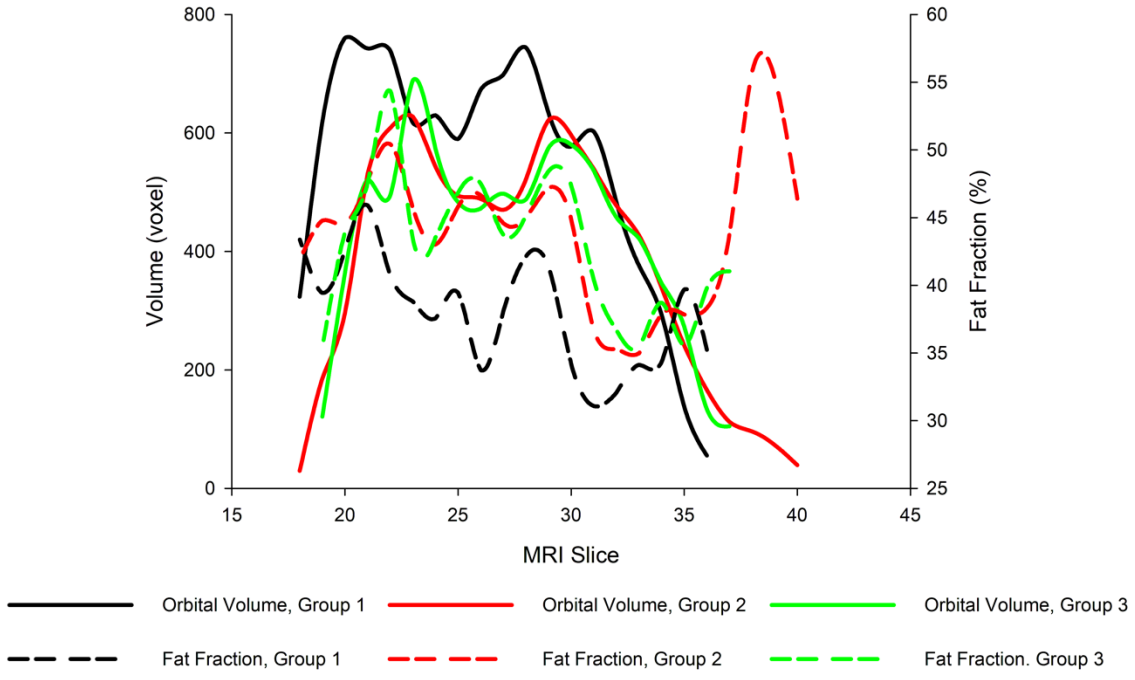

Average fat fraction and orbital fat volume per slice measured for the three MRI scans of the left orbit.

Figure 14. Left Orbit Fat Fraction Profile

Chapter 4. Discussion

Study Goals

The purpose of this study was to begin the process of establishing TED as a terrestrial analogue of SANS based on a recently published hypothesis of orbital congestion as the underlying mechanism (Reilly et al., 2023). This unifying hypothesis of orbital congestion is theorized to happen in astronauts during long-duration spaceflight, with the cephalad fluid shift in microgravity causing increased edema in orbital adipose tissue. The edema creates compression of the orbital structures by directing force against the posterior globe. The first aim of this study was to validate the performance of a q-Dixon MRI sequence to quantify fat-fraction of the orbital fat. The accuracy and repeatability of the sequence were evaluated in ideal conditions on phantom models. In the second aim, the same MRI sequence quantified fat-water fraction in the orbits of a preliminary human subject with TED. These two aims represent critical foundational work, on which future aspects of this study can build.

Phantom Model Validation

First, we confirmed the accuracy of the fat-water MRI sequence using orbital phantoms. This initial step was critical because it established the accuracy and precision of the MRI sequence over multiple scans and with different positions of the phantom models. Each of the three tested positions had good test-retest reliability, as each triplicate scan had a strong linear association with the true fat values (Figure 8).

Likewise, the MRI sequence produced accurate results, compared to true fat values, when measuring fat-fraction in all three tested positions. Analysis of absolute average deviation of the phantom model measured values from true fat values showed that the standard deviation was under 7% of the mean for all three positions. This result demonstrates the low variability of the measured fat-fraction in the phantoms, compared to the true fat-fractions of the phantoms. Overall, the results in the phantoms confirmed the accuracy and test-retest reliability of the MRI sequence. Moving forward we can be confident in the reliability and accuracy of data collected from human subjects.

Fat-water phantom modeling has been used to test MRI sequences before, although the initiation of planning and research in our study occurred before the publishing of these phantom modeling studies. One multi-site study by Hu et al. assessed the ability of q-Dixon Chemical Shift Encoded (CSE) sequencing in MRI scanners from three vendors (GE Healthcare, Siemens, and Philips) to quantify Calimetrix phantoms ranging from 0%-100% fat-fraction, with an emphasis on 0%-50% fat (Hu et al., 2021). Their results found a strong linear relationship between true and measured fat-fraction from all three devices. A later study by Hu et al. used phantom models ranging from 0%-100% fat, this time focusing on fat >60%, to test CSE Multi-echo Dixon based techniques and the repeatability and accuracy of this sequence across multiple MRI systems, vendors, and sites (Hu et al., 2024). Again, all three vendors showed good accuracy, compared to true values, and were highly reproducible. Results from both studies were consistent with ours in terms of finding good accuracy and repeatability,

further supporting the authenticity of our q-Dixon sequence validation with phantom models.

Preliminary Human Subject Imaging

Next, we used our validated q-Dixon MRI sequence to establish the reliability of fat-fraction imaging on the first-enrolled subject with TED. Pre-treatment imaging was done to simulate the development of SANS in astronauts, and while post-treatment imaging was unable to be done for this initial subject, this mimics the pre-flight baseline of astronauts before the development of SANS. Of the triplicate scans taken of the right orbit, the third scan produced a significantly higher weighted fat fraction per slice than the first scan. Similarly, the third scan had a significantly higher weighted fat fraction per slice than the second scan in the left orbit. No other comparisons were significantly different between the orbits. Despite the significant differences in fat fraction per slice between the third slice and slices one (right orbit) and two (left orbit), the COV for weighted fat fraction between scans was low, 6% in the right orbit and 7% in the left orbit. These results suggest generally good agreement between the three scans. When comparing imaging of the two orbits (Figure 11 and Figure 12), there was no statistical difference between the right and left orbits for weighted fat fraction and for orbital fat volume, which suggests edema and orbital adipose tissue were symmetric between the two orbits and that the first treatment subject was bilaterally affected by TED. This finding also indicates the manual processing done to determine the volume of the orbital fat in ImageJ was consistent between the two orbits. That there is no significant

difference between the fat-fraction measured in the right and left orbits is another indication the MRI sequence is repeatable within a human subject.

We also plotted fat-fraction and orbital fat volume as functions of MRI slice in the right orbit (Figure 13) and in the left orbit (Figure 14). Each scan in both orbits produced a biphasic relationship between scan number, which is an indicator of position within the orbit, and orbital fat volume. The biphasic shape of the relationship between slice and fat volume originates in the components of the orbital space. As the MRI sequence scans axially through the orbital space in the inferior to superior direction, each slice has a greater fat volume than the one preceding it. Then, approximately midway through the orbit, MRI sequence encounters the optic nerve and the EOMs. Only orbital fat was included when selecting ROIs during processing with ImageJ, and the optic nerve and EOMs were excluded, so the slice fat volume in these scans decreases compared to the peak. When the sequence moves past the optic nerve and EOMs, the fat volume of each slice increase again before falling off as the sequence moves out of the orbit. The fat fraction graphed per slice shows percentages of fat were highest in low slice numbers and fluctuates as the slice number increases. This also corresponds to the orbital location scanned and exclusion of other orbital contents such as EOMs and the optic nerve. For both the right and left orbits, several peaks of the fat-fraction percentage were at 45-50%, though there was variation throughout.

Although the general relationship between fat volume and slice number were similar for all scans in both orbits, it is important to note that one sequence was shifted on each side. In the right orbit, the third sequence is shifted right (Figure 13), and the first

sequence is shifted left in the left orbit (Figure 14). During imaging, the subject was instructed to stay stationary and to hold her breath while the scans were acquired. Each axial scan acquired images in 48 slices starting from the inferior orbit before moving through the superior orbit. If the subject was motionless in between and during each scan, the acquisitions would scan the contents of the orbit with the same slice number each time. It follows that the slice numbers of the shifted sequences in both orbits do not correspond with the slice numbers of the aligned sequences. The likely origin of the misalignment is head movement by the subject in between sequences (Figure 15).

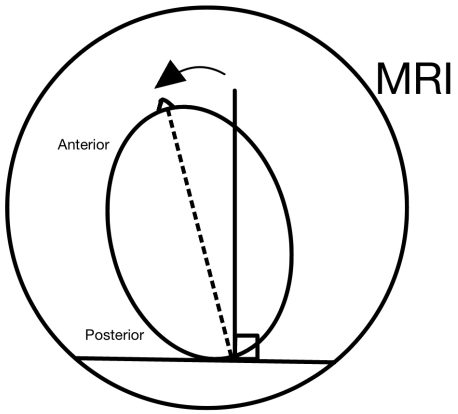

The circle represents the MRI machine, with the oval inside representing the alignment of a human subject's head. Normal alignment is perpendicular to the MRI table. The representation of a subject's head is shifted obliquely, with the dashed line representing the direction the head moved.

Figure 15. Demonstration of Misaligned Head

Figures 13 and 14 also demonstrate that MRI slices through the right and left eyes did not bisect the orbits at the same height. This effect can be appreciated when comparing the biphasic curves of the right and left orbital fat volume. The right orbit is acquired around slice 15, but the left orbit starts around slice 18. This artifact was another indication of subject misalignment during imaging. Each sequence was intended to image the orbit through the axial plane, but, due to movement of the subject's head, several scans were slightly oblique to axial orientation. The fact that the sequence performed well (i.e., accurately with good repeatability) when the orbital phantoms were in an oblique orientation is a favorable indication that head orientation slightly different than the original position would not have a large effect on the fat fraction results.

Measurements of orbital fat volume were more variable than those of volume-weighted fat fraction. When comparing the repeatability of the three sequences within each orbit, the COV of orbital fat volume was nearly double that of weighted fat fraction. This relatively high variability may be attributed to human error while making the fat volume measurements. Quantification of weighted fat fraction was highly dependent on the outcomes of the MRI sequence and of ImageJ processing. Although the fat volume of the scan selected to assess was dependent on human judgement, the results of the fat-fraction measurements of the voxels selected in each slice was reliant on direct data from the MRI output. As another variable, the volume of the orbit varies according to the precise location imaged at that time. The orbit itself is roughly pyramidal in shape, with the base pointing into the head. Axial scans through the orbit cut through different amounts of tissue when imaged from inferior to superior orbit.

Contrarily, fat-water fractions should be relatively consistent when imaging the makeup of orbital fat. Initial weighted fat fraction percentages measured show promising preliminary results in the assessment of fat-water fractions reliably and accurately with q-Dixon MRI sequencing and demonstrate the congruity of the measured data. The overall average fat fraction of our first subject was 42.97% ± 2.68% in the right orbit and 42.08% ± 3.04% in the left orbit. Stated another way, approximately 57% of the right orbit was water, and approximately 58% of the left orbit was water.

Although caution must be used when interpreting data from one subject, our data can be compared against the results from Kaichi et al. (2016). This group used q-Dixon imaging to determine that the healthy control subjects had an orbital water content of around 22%. Water content ranged from 20% to almost 40% in patients with untreated TED (Kaichi et al., 2016; Kaichi et al., 2019). Our results were outside of this range, possibly due to several differences in methodology between our study and Kaichi et al. We tested an original multi-Echo CSE q-Dixon sequence, which had not been previously used to image the orbit. This sequence was developed to measure fat-water fraction in the liver. Kaichi et al used a variation of q-Dixon imaging with Fast Spin Echo (FSE) sequencing with an orbital-fat-selection strategy in which the average signal-intensity ratios of orbital fat and extraocular muscles were determined from a small region of interest within each of these ocular components. The signal-intensity ratios and their standard deviation then were used to separate areas of orbital fat from other ocular structures. This approach increases the consistency of selection but is less customizable in comparison to our study. Contrast the approach of Kaichi and colleagues to the one we

took, where orbital fat was selected through manual designation voxel by voxel using thresholding. Our approach allows for precision and control over the designation of orbital fat, which is our region of interest, but introduces human error. Both our results and those of Kaichi found high water content in TED subjects. This finding likely is due to edema in the orbital fat and EOMs caused by the accumulation of hydrophilic glycosaminoglycans that occurs in TED (Kaichi et al., 2016). This edema contributes to mechanical compression of the posterior globe (Agarwal & Khanam, 2024).

Measurements of Orbital Congestion in TED and the Potential for Use in SANS

There are similarities between the clinical presentation of TED and that of SANS. Signs and symptoms of TED including proptosis, lid chemosis, retracted eyelids, disc edema, choroidal folds, and hyperopic changes in refractive error (Chandrasekaran et al., 2006). They are largely due to increased orbital congestion in adipose tissue and EOMs (Kaichi et al., 2016). Similar signs and symptoms are present in SANS. Almost 50% of 300 astronauts surveyed by Mader et al. (2011) reported decreases in near vision. Observation of choroidal folds after long-duration spaceflight has occurred in over 20% of astronauts, and OCT imaging comparing pre- and post-flight images has detected some level of optic disc edema in nearly all astronauts tested (Lee et al., 2020). Because these are signs that can be tested both in TED and in SANS, assessing them in future studies will be helpful in the exploration of TED as a comparison to SANS.

The Frisén scale is the current standard for the clinical evaluation of optic nerve head edema. As such, it is a primary diagnostic tool for SANS (Lee et al., 2020), but there are limitations to using the Frisén scale to diagnose SANS. The Frisén scale is

based on distinguishable features of the optic disc and peripapillary nerve fiber layer, as imaged with fundus photography and with dilated examination. Manifest edema is graded on a scale of 0-5. Typically, the diagnosis of SANS requires at least Grade 1 disc edema, but most long-duration astronauts do not develop disc edema that qualifies as Grade 1 (Lee et al., 2020). Yet, some level of optic disc edema is found in most astronauts, even if it does not rise to the level of Grade 1, suggesting that there is a gradient in the pathology of SANS. Moreover, small amounts of disc edema can be associated with signs and symptoms of SANS (Lee et al., 2020). Thus, diagnostic criteria beyond the Frisén scale are needed to detect SANS with acceptable sensitivity. Given the proposed theory of orbital congestion, which pairs in terms of signs and symptoms with orbital congestion found in TED, the evaluation of SANS could be expanded by including tools and measurements used in TED. Fat-water fraction may be an important biomarker, but it has never been determined in astronauts before or after spaceflight. Measurements of proptosis, which have also not been taken before, could be valuable in the evaluation of additional signs that can be used in the diagnosis of SANS.

Limitations

One limitation of this study is that the selection of orbital regions of interest, in which orbital fat was quantified, required personal judgement. Identification of orbital fat in ImageJ, the image processing software, was sometimes difficult to judge, and processing the MRI images to obtain orbital fat-water fraction percentages relied heavily on individual discernment of orbital fat. There was no sharp delineation between retro-bulbar fat and fat located anterior to the globe in many areas. As a result, selection of

orbital fat relied on personal judgment. In the future, a dedicated algorithm to select orbital fat would help eliminate inaccuracies introduced through human error.

Another limitation of this study is the very small sample size; only one subject was imaged. Enrolling additional subjects with TED and additional pair-matched control subjects will allow for refinement of identification and measurement of orbital fat-water content and allow for comparisons between TED and control subjects. A large sample size will give a comprehensive view of this pathology as a ground-based analogue to SANS.

Conclusion and Future Study

Despite these limitations, this study provides promising preliminary results for the study of orbital congestion as a potential etiology of SANS. Using TED to experiment with orbital fat-water fraction MR imaging allows us to explore a possible ground-based parallel to the published hypothesis. Verification of the MR sequence for reliability and accuracy is essential to the validity of future studies in this line of research. We were able to measure fat-water fractions in an initial TED treatment subject with the phantom-validated MRI sequence. The ability to test this theory on Earth is important because it provides access to larger sample sizes than what is possible in space, it allows for longer studies than what is possible in space, and it provides a substantial cost benefit. With a planned increase in long-duration space travel, it is essential to understand the pathophysiology, detection, and management of SANS as possible in order to preserve visual function and the ability to execute mission-critical tasks in all crewmembers.

Now that we have preliminary evidence that q-Dixon Multi-Echo Chemical Shift Encoded MRI sequencing has the ability to measure fat-water fractions in the orbit, the next step in this line of research is to enroll additional participants, both cases with TED and pair-matched controls. A large sample size will facilitate further understanding of orbital congestion in TED, which in turn will allow us to test the fitness of TED as a ground-based analogue to SANS. Obtaining imaging of TED patients before and after treatment allows for the possiblity of comparison with astronauts diagnosed with SANS and their baselines before development of SANS. As another avenue for future investigation, measurements of orbital fat-water fractions can be taken before and after spaceflights to seek orbital congestion in astronauts returning from long-duration missions. This approach can be complicated by the low numbers of space-naïve astronauts, however. Astronauts have often been on previous missions, so there could potentially be anatomical changes relating to SANS beforehand correlating to previous exposure to microgravity (Lee et al., 2020). In addition, it would be difficult to mask clinicians on the mission history of astronauts while selecting orbital fat-water measurements, which could introduce basis (Lee et al., 2020).

In conclusion, the results of this study are tangible first steps towards the establishment of TED as a novel terrestrial analogue to SANS. Our analysis of phantom models and of an initial human participant demonstrates q-Dixon sequencing is possible to use in measurements of orbital fat. This result supports future use of the MRI sequence to quantify orbital fat fraction in the remaining study subjects. Furthermore, this testing

will allow for future examination of orbital congestion in TED as a ground-based analogue to what is proposed to occur in SANS.

References

Agarwal, A., & Khanam, S. (2024). Dysthyroid Optic Neuropathy. In *StatPearls*. StatPearls Publishing. Copyright © 2024, StatPearls Publishing LLC.

Amirova, L. E., Plehuna, A., Rukavishnikov, I. V., Saveko, A. A., Peipsi, A., & Tomilovskaya, E. S. (2021). Sharp Changes in Muscle Tone in Humans Under Simulated Microgravity. *Front Physiol*, *12*, 661922. https://doi.org/10.3389/fphys.2021.661922

Anderson, A. P., Babu, G., Swan, J. G., Phillips, S. D., Knaus, D. A., Toutain-Kidd, C. M., Zegans, M. E., Fellows, A. M., Gui, J., & Buckey, J. C. (2017). Ocular changes over 60 min in supine and prone postures. *J Appl Physiol (1985)*, *123*(2), 415-423. https://doi.org/10.1152/japplphysiol.00687.2016

Anderson, A. P., Butterfield, J. S., Subramanian, P. S., & Clark, T. K. (2018). Intraocular pressure and cardiovascular alterations investigated in artificial gravity as a countermeasure to spaceflight associated neuro-ocular syndrome. *J Appl Physiol (1985)*, *125*(2), 567-576. https://doi.org/10.1152/japplphysiol.00082.2018

Anderson, A. P., Swan, J. G., Phillips, S. D., Knaus, D. A., Kattamis, N. T., Toutain-Kidd, C. M., Zegans, M. E., Fellows, A. M., & Buckey, J. C. (2016). Acute effects of changes to the gravitational vector on the eye. *J Appl Physiol (1985)*, *120*(8), 939-946. https://doi.org/10.1152/japplphysiol.00730.2015

Chandrasekaran, S., Petsoglou, C., Billson, F. A., Selva, D., & Ghabrial, R. (2006). Refractive change in thyroid eye disease (a neglected clinical sign). *Br J Ophthalmol*, *90*(3), 307-309. https://doi.org/10.1136/bjo.2005.078295

Chen, L., Hu, H., Chen, H. H., Chen, W., Wu, Q., Wu, F. Y., & Xu, X. Q. (2021). Usefulness of two-point Dixon T2-weighted imaging in thyroid-associated ophthalmopathy: comparison with conventional fat saturation imaging in fat suppression quality and staging performance. *Br J Radiol*, *94*(1118), 20200884. https://doi.org/10.1259/bjr.20200884

de Kerviler, E., Leroy-Willig, A., Clement, O., & Frija, J. (1998). Fat suppression techniques in MRI: an update. *Biomed Pharmacother*, *52*(2), 69-75. https://doi.org/10.1016/S0753-3322(98)80006-1

Debnam, J. M., Koka, K., & Esmaeli, B. (2021). Extrathyroidal Manifestations of Thyroid Disease: Graves Eye Disease. *Neuroimaging Clin N Am*, *31*(3), 367-378. https://doi.org/10.1016/j.nic.2021.04.006

Delfaut, E. M., Beltran, J., Johnson, G., Rousseau, J., Marchandise, X., & Cotten, A. (1999). Fat Suppression in MR Imaging: Techniques and Pitfalls. *Radiographics*, *19*(2), 373-382. https://doi.org/10.1148/radiographics.19.2.g99mr03373

Friedman, D. I., & Jacobson, D. M. (2004). Idiopathic intracranial hypertension. *J Neuroophthalmol*, *24*(2), 138-145. https://doi.org/10.1097/00041327-200406000-00009

Greenwald, S. H., Macias, B. R., Lee, S. M. C., Marshall-Goebel, K., Ebert, D. J., Liu, J. H. K., Ploutz-Snyder, R. J., Alferova, I. V., Dulchavsky, S. A., Hargens, A. R.,

Stenger, M. B., & Laurie, S. S. (2021). Intraocular pressure and choroidal thickness respond differently to lower body negative pressure during spaceflight. *J Appl Physiol (1985)*, *131*(2), 613-620. https://doi.org/10.1152/japplphysiol.01040.2020

Handel, A., Stern, C., Jordan, J., Dietlein, T., Enders, P., & Cursiefen, C. (2021). Eye changes in space : New insights into clinical aspects, pathogenesis, and prevention. *Ophthalmologe*, *118*(Suppl 1), 96-101. https://doi.org/10.1007/s00347-020-01272-6 (Augenveranderungen im All : Aktuelles zu Klinik, Pathogenese und Pravention.)

Herranz, R., Anken, R., Boonstra, J., Braun, M., Christianen, P. C., de Geest, M., Hauslage, J., Hilbig, R., Hill, R. J., Lebert, M., Medina, F. J., Vagt, N., Ullrich, O., van Loon, J. J., & Hemmersbach, R. (2013). Ground-based facilities for simulation of microgravity: organism-specific recommendations for their use, and recommended terminology. *Astrobiology*, *13*(1), 1-17. https://doi.org/10.1089/ast.2012.0876

Hines, C. D., Yu, H., Shimakawa, A., McKenzie, C. A., Brittain, J. H., & Reeder, S. B. (2009). T1 independent, T2* corrected MRI with accurate spectral modeling for quantification of fat: validation in a fat-water-SPIO phantom. *J Magn Reson Imaging*, *30*(5), 1215-1222. https://doi.org/10.1002/jmri.21957

Hu, H. H., Chen, H. S.-M., & Hernando, D. (2024). Linearity and bias of proton density fat fraction across the full dynamic range of 0–100%: a multiplatform, multivendor phantom study using 1.5T and 3T MRI at two sites. *Magnetic Resonance Materials in Physics, Biology and Medicine*. https://doi.org/10.1007/s10334-024-01148-9

Hu, H. H., Yokoo, T., Bashir, M. R., Sirlin, C. B., Hernando, D., Malyarenko, D., Chenevert, T. L., Smith, M. A., Serai, S. D., Middleton, M. S., Henderson, W. C., Hamilton, G., Shaffer, J., Shu, Y., Tkach, J. A., Trout, A. T., Obuchowski, N., Brittain, J. H., Jackson, E. F., . . . Committee, R. Q. I. B. A. P. B. (2021). Linearity and Bias of Proton Density Fat Fraction as a Quantitative Imaging Biomarker: A Multicenter, Multiplatform, Multivendor Phantom Study. *Radiology*, *298*(3), 640-651. https://doi.org/10.1148/radiol.2021202912

Kaichi, Y., Tanitame, K., Itakura, H., Ohno, H., Yoneda, M., Takahashi, Y., Akiyama, Y., & Awai, K. (2016). Orbital Fat Volumetry and Water Fraction Measurements Using T2-Weighted FSE-IDEAL Imaging in Patients with Thyroid-Associated Orbitopathy. *AJNR Am J Neuroradiol*, *37*(11), 2123-2128. https://doi.org/10.3174/ajnr.A4859

Kaichi, Y., Tanitame, K., Terada, H., Itakura, H., Ohno, H., Yoneda, M., Takahashi, Y., Akiyama, Y., & Awai, K. (2019). Thyroid-associated Orbitopathy: Quantitative Evaluation of the Orbital Fat Volume and Edema Using IDEAL-FSE. *Eur J Radiol Open*, *6*, 182-186. https://doi.org/10.1016/j.ejro.2019.05.003

Killer, H. E., Jaggi, G. P., Flammer, J., Miller, N. R., Huber, A. R., & Mironov, A. (2007). Cerebrospinal fluid dynamics between the intracranial and the subarachnoid space of the optic nerve. Is it always bidirectional? *Brain*, *130*(Pt 2), 514-520. https://doi.org/10.1093/brain/awl324

Lacheta, D., Miskiewicz, P., Gluszko, A., Nowicka, G., Struga, M., Kantor, I., Poslednik, K. B., Mirza, S., & Szczepanski, M. J. (2019). Immunological Aspects of Graves' Ophthalmopathy. *Biomed Res Int*, *2019*, 7453260. https://doi.org/10.1155/2019/7453260

Laurie, S. S., Greenwald, S. H., Marshall-Goebel, K., Pardon, L. P., Gupta, A., Lee, S. M. C., Stern, C., Sangi-Haghpeykar, H., Macias, B. R., & Bershad, E. M. (2021). Optic disc edema and chorioretinal folds develop during strict 6 degrees head-down tilt bed rest with or without artificial gravity. *Physiol Rep*, *9*(15), e14977. https://doi.org/10.14814/phy2.14977

Laurie, S. S., Lee, S. M. C., Macias, B. R., Patel, N., Stern, C., Young, M., & Stenger, M. B. (2020). Optic Disc Edema and Choroidal Engorgement in Astronauts During Spaceflight and Individuals Exposed to Bed Rest. *JAMA Ophthalmol*, *138*(2), 165-172. https://doi.org/10.1001/jamaophthalmol.2019.5261

Lawley, J. S., Petersen, L. G., Howden, E. J., Sarma, S., Cornwell, W. K., Zhang, R., Whitworth, L. A., Williams, M. A., & Levine, B. D. (2017). Effect of gravity and microgravity on intracranial pressure. *J Physiol*, *595*(6), 2115-2127. https://doi.org/10.1113/JP273557

Lee, A. G., Mader, T. H., Gibson, C. R., Tarver, W., Rabiei, P., Riascos, R. F., Galdamez, L. A., & Brunstetter, T. (2020). Spaceflight associated neuro-ocular syndrome (SANS) and the neuro-ophthalmologic effects of microgravity: a review and an update. *NPJ Microgravity*, *6*, 7. https://doi.org/10.1038/s41526-020-0097-9

Macias, B. R., Patel, N. B., Gibson, C. R., Samuels, B. C., Laurie, S. S., Otto, C., Ferguson, C. R., Lee, S. M. C., Ploutz-Snyder, R., Kramer, L. A., Mader, T. H., Brunstetter, T., & Stenger, M. B. (2020). Association of Long-Duration Spaceflight With Anterior and Posterior Ocular Structure Changes in Astronauts and Their Recovery. *JAMA Ophthalmol*, *138*(5), 553-559. https://doi.org/10.1001/jamaophthalmol.2020.0673

Mader, T. H., Gibson, C. R., Miller, N. R., Subramanian, P. S., Patel, N. B., & Lee, A. G. (2019). An overview of spaceflight-associated neuro-ocular syndrome (SANS). *Neurol India*, *67*(Supplement), S206-S211. https://doi.org/10.4103/0028-3886.259126

Mader, T. H., Gibson, C. R., Otto, C. A., Sargsyan, A. E., Miller, N. R., Subramanian, P. S., Hart, S. F., Lipsky, W., Patel, N. B., & Lee, A. G. (2017). Persistent Asymmetric Optic Disc Swelling After Long-Duration Space Flight: Implications for Pathogenesis. *J Neuroophthalmol*, *37*(2), 133-139. https://doi.org/10.1097/WNO.0000000000000467

Mader, T. H., Gibson, C. R., Pass, A. F., Kramer, L. A., Lee, A. G., Fogarty, J., Tarver, W. J., Dervay, J. P., Hamilton, D. R., Sargsyan, A., Phillips, J. L., Tran, D., Lipsky, W., Choi, J., Stern, C., Kuyumjian, R., & Polk, J. D. (2011). Optic disc edema, globe flattening, choroidal folds, and hyperopic shifts observed in astronauts after long-duration space flight. *Ophthalmology*, *118*(10), 2058-2069. https://doi.org/10.1016/j.ophtha.2011.06.021

Marshall-Goebel, K., Mulder, E., Bershad, E., Laing, C., Eklund, A., Malm, J., Stern, C., & Rittweger, J. (2017). Intracranial and Intraocular Pressure During Various Degrees of Head-Down Tilt. *Aerosp Med Hum Perform*, *88*(1), 10-16. https://doi.org/10.3357/AMHP.4653.2017

Morgan, W. H., Balaratnasingam, C., Lind, C. R., Colley, S., Kang, M. H., House, P. H., & Yu, D. Y. (2016). Cerebrospinal fluid pressure and the eye. *Br J Ophthalmol*, *100*(1), 71-77. https://doi.org/10.1136/bjophthalmol-2015-306705

Nelson, E. S., Mulugeta, L., & Myers, J. G. (2014). Microgravity-induced fluid shift and ophthalmic changes. *Life (Basel)*, *4*(4), 621-665. https://doi.org/10.3390/life4040621

Ollitrault, A., Charbonneau, F., Herdan, M. L., Berges, O., Zuber, K., Giovansili, L., Launay, P., Savatovsky, J., & Lecler, A. (2021). Dixon-T2WI magnetic resonance imaging at 3 tesla outperforms conventional imaging for thyroid eye disease. *Eur Radiol*, *31*(7), 5198-5205. https://doi.org/10.1007/s00330-020-07540-y

Oreskovic, D., & Klarica, M. (2010). The formation of cerebrospinal fluid: nearly a hundred years of interpretations and misinterpretations. *Brain Res Rev*, *64*(2), 241-262. https://doi.org/10.1016/j.brainresrev.2010.04.006

Pletser, V., Gharib, T., Gai, F., Mora, C., & Rosier, P. (2009). The 50 parabolic flight campaigns of the European Space Agency to conduct short duration microgravity research experimentation. Conference: 60th IAF Congress (Daejeon, Korea: Congress Paper of the International Austronauts Federation). Paper: IAC-09-A2,

Reilly, M. A., Katz, S. E., & Roberts, C. J. (2023). Orbital fat swelling: A biomechanical theory and supporting model for spaceflight-associated neuro-ocular syndrome (SANS). *Front Bioeng Biotechnol*, *11*, 1095948. https://doi.org/10.3389/fbioe.2023.1095948

Shinojima, A., Kakeya, I., & Tada, S. (2018). Association of Space Flight With Problems of the Brain and Eyes. *JAMA Ophthalmol*, *136*(9), 1075-1076. https://doi.org/10.1001/jamaophthalmol.2018.2635

Stenger, M. B., Tarver, W. J., Brunstetter, T., Gibson, C. R., Laurie, S. S., Lee, S., Macias, B. R., Mader, T. H., Otto, C., & Smith, S. M. (2017). *Evidence report: risk of spaceflight associated neuro-ocular syndrome (SANS)*.

Watkins, W., Hargens, A. R., Seidl, S., Clary, E. M., & Macias, B. R. (2017). Lower-body negative pressure decreases noninvasively measured intracranial pressure and internal jugular vein cross-sectional area during head-down tilt. *J Appl Physiol (1985)*, *123*(1), 260-266. https://doi.org/10.1152/japplphysiol.00091.2017

Zhai, L., Luo, B., Wu, H., Wang, Q., Yuan, G., Liu, P., Ma, Y., Zhao, Y., & Zhang, J. (2021). Prediction of treatment response to intravenous glucocorticoid in patients with thyroid-associated ophthalmopathy using T2 mapping and T2 IDEAL. *European Journal of Radiology*, *142*, 109839. https://doi.org/https://doi.org/10.1016/j.ejrad.2021.109839